JOURNAL OF SPACECRAFT AND ROCKETS
Vol. 51, No. 5, September–October 2014

Laser Reference Sensor Alignment Estimation Using Star Observations

Noah H. Smith,* Sungkoo Bae,† and Bob E. Schutz‡
University of Texas at Austin, Austin, Texas 78712

DOI: 10.2514/1.A32669

The laser reference sensor is the central instrument in the Ice, Cloud, and Land Elevation Satellite laser pointing knowledge system, simultaneously observing stars and the altimetry laser in a single instrument coordinate frame. The star measurements are sparse, with the intermittent tracking of individual stars because of the small field of view and no tracking in sunlight due to problems with scattered light. Attitude estimation for the laser reference sensor alone is challenging due to its limited stellar data output. There are also three commercial star trackers mounted on the science instrument and spacecraft bus. The time-varying alignments and attitudes of all four star trackers are tracked simultaneously using an alignment filter in order to determine the stability of the laser reference sensor and the effects of its sparse star observations on alignment and attitude knowledge. The filter is able to predict laser reference sensor star measurements with accuracies of approximately 0.5 to 1.5 arcseconds over time scales greater than the orbital period while tracking laser reference sensor alignment variations on the order of 40 arcseconds.

Nomenclature

$A_i^b(t)$	=	attitude rotation from inertial frame to body frame
A_b^{TRK}	=	constant reference alignment rotation from body frame
$A_i^{\mathrm{TRK}}(t)$	=	attitude rotation from inertial frame to a tracker frame (tracker = laser reference sensor, instrument star tracker, bus star tracker 1, or bus star tracker 2)
$\boldsymbol{a}(t)$	=	attitude error rotation vector with $a \equiv \lvert a \rvert$, rad
$\boldsymbol{a}_{\mathrm{TRK}}(t)$	=	alignment rotation vector
$\boldsymbol{b}(t)$	=	gyro rate bias vector, rad/s
H	=	sensitivity matrix
H_i	=	filter bank $i = 1, \ldots, n$ of candidate σ_{TRK} values
$h(u)$	=	measurement model
$\boldsymbol{h}$	=	unit vector horizontal and vertical coordinates in i, j, k frame
i, j, k	=	sensor or local tangent plane frame axes for expressing unit vectors
K	=	Kalman gain matrix
P	=	state covariance matrix
Q	=	process noise covariance matrix
$q(a(t))$	=	unit-norm attitude error quaternion function of $a(t)$ with $\lvert q(a(t)) \rvert = 1$
$q_{\mathrm{ref}}(t)$	=	reference attitude quaternion with $\lvert q_{\mathrm{ref}}(t) \rvert = 1$
R	=	measurement noise covariance matrix
$R(a)$	=	state transition submatrix
$S(a)$	=	state transition submatrix
$\boldsymbol{u}$	=	three-dimensional unit vector
$\boldsymbol{x}(t)$	=	state vector
x, y, z	=	body frame axes
$\Delta h, \Delta v$	=	observed minus predicted star residuals
$\eta(t)$	=	zero-mean Gaussian noise process
σ_{TRK}	=	alignment process noise
Φ	=	state transition matrix
$\boldsymbol{\omega}(t)$	=	angular rate vector, rad/s
$\boldsymbol{\omega}_g(t)$	=	gyro output angular rate vector, rad/s

Received 31 March 2013; revision received 27 June 2013; accepted for publication 9 July 2013; published online 14 February 2014.

*Postdoctoral Fellow, Center for Space Research. Member AIAA.
†Research Scientist Engineer, Center for Space Research. Member AIAA.
‡Associate Director, Center for Space Research. Associate Fellow AIAA.

I. Introduction

THE Ice, Cloud, and Land Elevation Satellite (ICESat) is a member of the NASA Earth Observing System. It was launched in January 2003 and deorbited in August 2010. The primary objective was laser altimetry using the Geoscience Laser Altimeter System (GLAS) for the determination of polar ice sheet mass balances and their contribution to global sea-level change, requiring highly accurate measurements of the surface elevation at each laser footprint [1–3]. The location of a footprint and its associated elevation were obtained by combining the geocentric position vector of GLAS, the laser pointing vector, and laser pulse time-of-flight measurements. The accuracy requirement for surface elevation is 15 cm and is equivalent to a laser pointing knowledge accuracy of 1.5 arcseconds.

The pointing knowledge system centers on a laser reference sensor (LRS), which simultaneously observes stars and the altimetry laser in the LRS coordinate frame [4–7]. Ideally, the LRS star observations determine the LRS attitude and, by extension, the pointing of the laser vector in the celestial frame. The estimation of the LRS attitude is the key step in tying the LRS laser observations to the celestial frame, but unfortunately the LRS star observations are sparse due to design tradeoffs and functional limitations (Sec. II).

ICESat also carried three commercial off-the-shelf star trackers. The instrument star tracker (IST) was mounted beside the LRS on GLAS along with a gyro unit. Two bus star trackers (BST1 and BST2) were mounted on the spacecraft. To bypass the limitations of the LRS, its star observations were intended to be combined with those from the IST based on an alignment reference signal linking the LRS and IST coordinate frames. The reference signal used a portion of the 532 nm wavelength signal from the primary altimetry laser beam, which had both 532 nm and 1064 nm components. The 532 nm signal energy was severely degraded early in the mission, and the reference signal was effectively lost. Without the reference signal, alternative LRS attitude estimation methods involving some or all of the other three trackers and gyros were necessary. The original LRS attitude estimation method and an alternative using the IST and gyro unit alone are described in [8].

The LRS attitude estimation method used here simultaneously filtered the observations from all four star trackers to estimate their time-varying alignments and attitudes, effectively combining the LRS, IST, BST1, and BST2 star observations. This type of filter is referred to as an alignment filter or alignment Kalman filter [9]. The motivation was to produce an adequate estimate of the LRS alignment relative to the other three star trackers for inferring the LRS attitude independently from the lost reference signal. Within the alignment filter, the LRS star observations were only used to update the LRS alignment estimate. If the LRS alignment variations were not too large or fast, the sparse LRS star observations were able to provide

adequate information for updating the alignment estimate. The alignment filter approach essentially took advantage of the fact that the LRS alignment was relatively constant compared to the LRS attitude.

Alignment filtering has been discussed in the literature since 1990 [10–15], particularly by Pittelkau et al. since 2000 [9,16–20]. Currently, the main conceptual questions concern the definition of the body frame. If it is practical to identify the body frame with the gyro unit, then the relative motion of every star tracker is observable [17]. The more conservative approach adopted here is to identify the body frame with a star tracker, making its relative motion unobservable. Flight experiences and flight data from Thermosphere, Ionosphere, Mesosphere Energetics and Dynamics (TIMED), Mercury Surface, Space Environment, Geochemistry, and Ranging (MESSENGER), and Space Infrared Telescope Facility (SIRTF) are discussed in [18–21]. TIMED and MESSENGER can be classed as baseline examples involving two identical collocated star trackers. ICESat is a more complex case because of the number, types, and locations of its star trackers. SIRTF is a particularly sophisticated application that extends the filter state to include calibration parameters for various science instruments.

A contribution of this paper is an investigation of the effects of the sparse LRS star observations on alignment filtering. There is a qualitative difference or asymmetry between the information throughput of the LRS and the other three star trackers. The effects depend on the time scales and accuracies needed to meet the altimetry science requirements. The results are represented here by overall accuracies for the LRS alignment and attitude estimates over time scales greater than the orbital period.

Another contribution is a method for estimating the alignment process noise parameters. Alignment process noise should reflect the uncertainty due to true alignment variations over relevant time scales. The focus here is on time scales greater than the orbital period, during which the sparse LRS star observations provide adequate information to track LRS alignment variations. The alignment process noise parameters are estimated using multiple-model adaptive estimation (MMAE).

There has been discussion in the literature of alignment filtering for inferring structural alignment between the payload and bus but few examples of flight experience (possibly SIRTF alone). In principle, the alignment of GLAS with respect to the bus is observable due to the presence of two star trackers on each, making it possible to use alignment filtering for the knowledge of GLAS alignment stability. Evidence that the LRS to GLAS optical bench alignment is stable, implying that LRS alignment variations reflect GLAS optical bench alignment variations, is provided in [8]. It will be shown here that alignment filter results provide evidence of significant LRS and GLAS alignment variations.

II. Hardware Background and Coordinate Definitions

Figure 1 shows the four star tracker line-of-sight unit vectors in the x, y, z body frame. The LRS and IST lines of sight are parallel to the z axis.

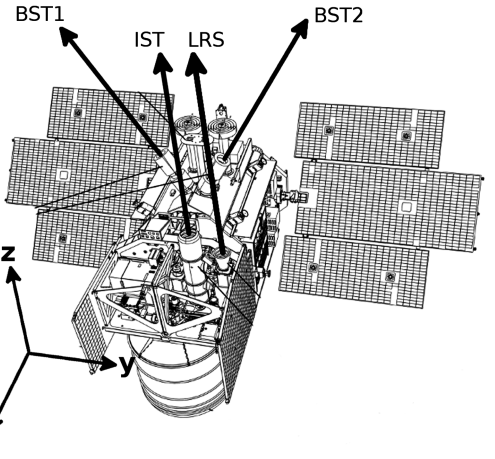

Fig. 1 The four ICESat star tracker line-of-sight unit vectors in the body frame.

The BST1 and BST2 lines of sight are angled 30 deg from the z axis in the y, z plane. The body frame is associated with the spacecraft bus and with BST1, in particular. In practice, the body frame is defined here by the estimated BST1 attitude and a constant BST1 reference alignment. It will be shown that BST alignment variations are on the order of a few arcseconds and that the BST1 coordinate frame is an adequate proxy for a body frame in which to track the LRS and IST alignments.

The LRS and IST are mounted side by side on the GLAS optical bench along with a space inertial reference unit (SIRU) gyro unit as shown on the left side of Fig. 2. The right side of Fig. 2 is a schematic of the instruments on the plane of the optical bench. Variations of the GLAS optical bench to the bus alignment can ideally be observed as correlated variations of the LRS and IST line-of-sight vectors relative to the BST1 and BST2 line-of-sight vectors.

The LRS concept can be implemented in a variety of ways. For example, two trackers can be joined stably so that their coordinate frames are effectively combined. Combining their output in a single data stream creates a tracker with two fields of view: one to track the laser and one to track stars. The implementation of the GLAS LRS is based on a single optical train and tracking unit. The tracking unit is from a commercial off-the-shelf star tracker. High angular resolution, with the tradeoff of a small field of view, is needed to achieve the required pointing knowledge accuracy. To make more stars acquirable, the sensitivity is increased by using optics with larger apertures. The hardware modifications are implemented in custom optics (Fig. 2) and a custom sun shade resulting in a 0.5 deg square field of view and an instrument magnitude limit of 7.5. Three spots of light are observed and tracked: a laser spot, a reference spot from the Collimated Reference Source (CRS), and an intermittent star spot.

Because of the small field of view, at most, one star spot is tracked at a time, and there are long gaps between stars. When the LRS was

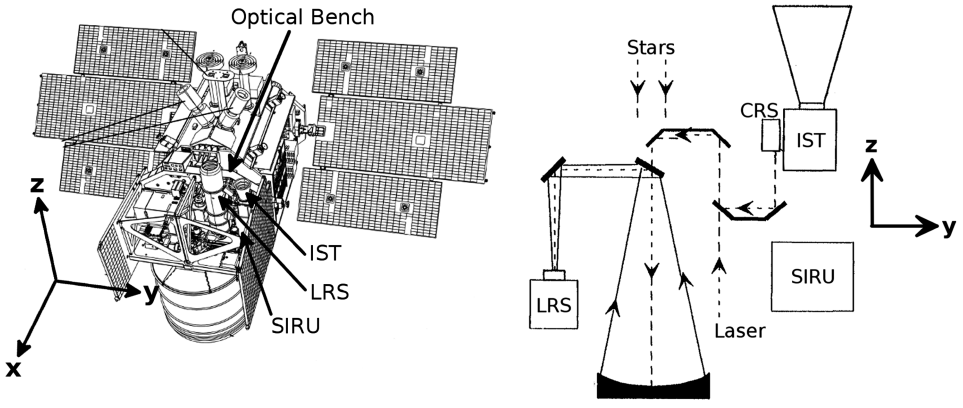

a) b)

Fig. 2 a) GLAS instruments and b) schematic of the GLAS optical bench in the body frame.

activated on orbit, there were frequent system resets attributed to stray light bypassing or scattering from the sun shade. The resets were initially avoided by deactivating the LRS while in sunlight. The LRS software was eventually modified to deactivate star tracking in sunlight. The result is intermittent LRS observations of individual stars while in eclipse and none while in sunlight. Attitude estimation using the LRS and gyros alone is relatively difficult due to the limited celestial information. For example, an initial attitude estimate for sequential filtering has to come from a source other than the LRS since single-frame attitude determination requires simultaneous observations of two or more stars. Once the filter is initialized and converged, the measurement updates from the LRS are intermittent at best.

The IST and BSTs have 8-by-8 deg fields of view and 10 Hz output. The IST is an HD-1003 and tracks up to six stars with an instrument magnitude limit of 6.2. The LRS tracking unit is taken from an HD-1003 identical to the IST. The BSTs are CT-602s and track up to five stars with an instrument magnitude limit of 7.1. The spacecraft telemetry includes 10 Hz samples of the 100 Hz SIRU output. The spacecraft is nadir pointing with an angular rate of 223 arcseconds/s about its pitch axis (orbit normal axis), with periodic pitch and roll rate deviations for calibration ocean scans (3 deg off nadir) and intermittent deviations for target-of-opportunity pointing (<5 deg off nadir). The pitch axis is aligned (approximately parallel or antiparallel) with the body frame x axis in the flight data used here, and the yaw axis and zenith direction are aligned with the body frame z axis. The four star tracker lines of sight follow one another along a great circle of the sky except for small deviations during ocean scans and target-of-opportunity pointing.

Local tangent plane coordinates are used here to represent clusters of two or more nearby unit vectors and take advantage of the body frame geometry. One unit vector from the cluster is defined as a reference $\boldsymbol{u}_{\text{ref}}$, around which a local i, j, k coordinate frame is formed by

$$k = \boldsymbol{u}_{\text{ref}} \tag{1}$$

$$j = \boldsymbol{u}_{\text{ref}} \times x \tag{2}$$

$$i = j \times k \tag{3}$$

Unit vectors are expressed in an i, j, k local tangent plane frame by $\boldsymbol{u} = [\,u_i \quad u_j \quad u_k\,]^T$ or angles θ_h and θ_v from the k axis toward the i and j axes. An intermediate vector $\boldsymbol{u}' = [\,\boldsymbol{h} \quad \boldsymbol{v} \quad 1\,]^T$ is defined, where

$$\boldsymbol{h} \equiv \tan\theta_h = u_i/u_k \tag{4}$$

$$\boldsymbol{v} \equiv \tan\theta_v = u_j/u_k \tag{5}$$

and $\boldsymbol{u} = \boldsymbol{u}'/\|\boldsymbol{u}'\|$. The i, j plane is locally tangent to the unit sphere around the body frame origin at the point $k \equiv \boldsymbol{u}_{\text{ref}}$. Near $\boldsymbol{u}_{\text{ref}}$, $\boldsymbol{h} \cong \theta_h$ and $\boldsymbol{v} \cong \theta_v$ and the local tangent plane coordinates are approximately equivalent to angles. The i axis points as directly as possible within the tangent plane toward the body frame x axis, and the h coordinate represents a rotation from $\boldsymbol{u}_{\text{ref}}$ toward or away from the body frame x axis, depending on the sign. Correlations of the local tangent plane $\boldsymbol{h}$, $\boldsymbol{v}$ coordinates representing line-of-sight variations and measurement residuals (star predictions and observations) are used here to characterize the alignment filter results.

III. Alignment Filter

An alignment filter is used to simultaneously predict the measurements from all four star trackers. The sparse LRS observations are effectively combined with the observations from the other three trackers. The measurement residuals are used to update the filter states, which represent the body frame attitude and time-varying corrections to reference alignments for three of the trackers (LRS, IST, and BST2). The fourth tracker (BST1) is tied to the body frame by a constant reference alignment. The combined states represent the attitudes of all four trackers. This type of alignment filtering is applicable to any configuration of vector sensors. If the vector observations can be predicted, then the sensor alignments can be corrected.

The notation A is used here for rotation matrices (direction cosine matrices) because they usually represent either an attitude or alignment. Rotation vectors $\boldsymbol{a}$ are also used for alignment. A rotation vector is defined as a Euler axis and angle $a = \phi e$; $|e| = 1$ [22]. The rotation matrix A equivalent to a rotation vector $\boldsymbol{a}$ is $A(a)$. An overhat $\hat{x}$ designates an estimate of the truth x.

A. Attitude, State, and Covariance

The BST1 attitude is modeled as the product of the BST1 reference alignment A_b^{BST1} and the body frame attitude $A_i^b(t)$,

$$A_i^{\text{BST1}}(t) = A_b^{\text{BST1}} A_i^b(t) \tag{6}$$

Time-varying corrections to A_b^{BST1} are not modeled or estimated, and the BST1 coordinate frame is effectively identified with the body frame. Time-varying rotation vectors $\boldsymbol{a}_{\text{TRK}}(t)$ representing small alignment corrections are included in the attitude models for the other trackers,

$$A_i^{\text{LRS}}(t) = A(\boldsymbol{a}_{\text{LRS}}(t)) A_b^{\text{LRS}} A_i^b(t) \tag{7}$$

$$A_i^{\text{IST}}(t) = A(\boldsymbol{a}_{\text{IST}}(t)) A_b^{\text{IST}} A_i^b(t) \tag{8}$$

$$A_i^{\text{BST2}}(t) = A(\boldsymbol{a}_{\text{BST2}}(t)) A_b^{\text{BST2}} A_i^b(t) \tag{9}$$

where $A(\boldsymbol{a}_{\text{TRK}}(t))$ is the rotation matrix equivalent of the rotation vector $\boldsymbol{a}_{\text{TRK}}(t)$ and A_b^{TRK} is a reference alignment.

The state vector is

$$\boldsymbol{x}(t) = [\,\boldsymbol{a}(t)^T \quad \boldsymbol{b}(t)^T \quad \boldsymbol{a}_{\text{LRS}}(t)^T \quad \boldsymbol{a}_{\text{IST}}(t)^T \quad \boldsymbol{a}_{\text{BST2}}(t)^T\,]^T \tag{10}$$

where $\boldsymbol{a}(t)$ is the body frame attitude error rotation vector and $\boldsymbol{b}(t)$ is the gyro rate bias. These states are estimated sequentially using an alignment filter based on the standard attitude filter, referred to by [22] as the multiplicative extended Kalman filter. The description here follows [9,17,22,23].

The filter performs an unconstrained estimation of $\boldsymbol{a}(t)$ during each measurement update phase while maintaining the overall body frame attitude estimate in the unit-norm reference attitude quaternion $q_{\text{ref}}(t)$ and $\hat{A}_i^b(t) = A(q_{\text{ref}}(t))$. The true attitude $q(t)$ is modeled as $q(t) = q(\boldsymbol{a}(t)) \otimes q_{\text{ref}}(t)$, where $q(\boldsymbol{a}(t))$ is a unit-norm quaternion equivalent to the rotation vector $\boldsymbol{a}(t)$ and $\otimes$ denotes quaternion multiplication [22]. The measurement update phase assigns a finite value $\hat{\boldsymbol{a}}_+$ to $\hat{\boldsymbol{a}}(t)$ while the reference quaternion retains its preupdate value $q_{\text{ref},-}$. The update information is moved from $\hat{\boldsymbol{a}}_+$ to a postupdate reference $q_{\text{ref},+}$, and $\hat{\boldsymbol{a}}(t)$ is reset to zero so that $q(\hat{\boldsymbol{a}}_+) \otimes q_{\text{ref},-} = q(\boldsymbol{0}) \otimes q_{\text{ref},+}$.

The covariance matrix P is given by

$$P_{15\times15} \equiv E\{(x-\hat{x})(x-\hat{x})^T\} = \begin{bmatrix} P_a & P_{ab} & & & \\ P_{ab} & P_b & & & \\ & & P_{\text{LRS}} & & \\ & & & P_{\text{IST}} & \\ & & & & P_{\text{BST2}} \end{bmatrix} \tag{11}$$

where P is partitioned into 3×3 attitude error P_a, gyro rate bias P_b, correlation P_{ab}, and alignment P_{TRK} submatrices. In the continuous-time linearized state equation given by

$$\begin{bmatrix} \delta\dot{\boldsymbol{a}} \\ \delta\dot{\boldsymbol{b}} \\ \delta\dot{\boldsymbol{a}}_{\mathrm{LRS}} \\ \delta\dot{\boldsymbol{a}}_{\mathrm{IST}} \\ \delta\dot{\boldsymbol{a}}_{\mathrm{BST2}} \end{bmatrix} = \begin{bmatrix} -[\boldsymbol{\omega}_{\mathrm{ref}}\times] & I_{3\times3} & & & & \\ \mathbf{0}_{3\times3} & \mathbf{0}_{3\times3} & & & & \\ & & \mathbf{0}_{3\times3} & & & \\ & & & \mathbf{0}_{3\times3} & & \\ & & & & \mathbf{0}_{3\times3} & \\ & & & & & \mathbf{0}_{3\times3} \end{bmatrix} \begin{bmatrix} \delta\boldsymbol{a} \\ \delta\boldsymbol{b} \\ \delta\boldsymbol{a}_{\mathrm{LRS}} \\ \delta\boldsymbol{a}_{\mathrm{IST}} \\ \delta\boldsymbol{a}_{\mathrm{BST2}} \end{bmatrix} + I_{15\times15} \begin{bmatrix} \eta_{\mathrm{ARW}} \\ \eta_{\mathrm{RRW}} \\ \eta_{\mathrm{LRS}} \\ \eta_{\mathrm{IST}} \\ \eta_{\mathrm{BST2}} \end{bmatrix} \tag{12}$$

the gyro rate bias $\delta\boldsymbol{b}$ and alignments $\delta\boldsymbol{a}_{\mathrm{LRS}}$, $\delta\boldsymbol{a}_{\mathrm{IST}}$, and $\delta\boldsymbol{a}_{\mathrm{BST2}}$ are driven by process noise alone, with $E\{\eta_{\mathrm{ARW}} \quad \eta_{\mathrm{ARW}}^T\} = \sigma_{\mathrm{ARW}}^2 I$, $E\{\eta_{\mathrm{RRW}} \quad \eta_{\mathrm{RRW}}^T\} = \sigma_{\mathrm{RRW}}^2 I$, $E\{\eta_{\mathrm{LRS}} \quad \eta_{\mathrm{LRS}}^T\} = \sigma_{\mathrm{LRS}}^2 I$, $E\{\eta_{\mathrm{IST}} \quad \eta_{\mathrm{IST}}^T\} = \sigma_{\mathrm{IST}}^2 I$, and $E\{\eta_{\mathrm{BST2}} \quad \eta_{\mathrm{BST2}}^T\} = \sigma_{\mathrm{BST2}}^2 I$. The discrete-time process noise matrix for a propagation interval $\Delta t \equiv t_{k+1} - t_k$ is given by

$$Q_k(\Delta t) = \begin{bmatrix} (\sigma_{\mathrm{AWN}}^2 + \Delta t\sigma_{\mathrm{ARW}}^2 + (\Delta t^3/3)\sigma_{\mathrm{RRW}}^2)I & (\Delta t^2/2)\sigma_{\mathrm{RRW}}^2 I & & & & \\ (\Delta t^2/2)\sigma_{\mathrm{RRW}}^2 I & \Delta t\sigma_{\mathrm{RRW}}^2 I & & & & \\ & & \Delta t\sigma_{\mathrm{LRS}}^2 I & & & \\ & & & \Delta t\sigma_{\mathrm{IST}}^2 I & & \\ & & & & \Delta t\sigma_{\mathrm{BST2}}^2 I & \end{bmatrix} \tag{13}$$

Parameter estimates for the alignment process noises σ_{LRS}, σ_{IST}, and σ_{BST2} are the subject of Sec. III.D.

B. Propagation

The gyro unit outputs time-tagged angular increments, which are used to compute the rate vector $\boldsymbol{\omega}_g(t)$. The true rate $\boldsymbol{\omega}(t)$ is modeled by $\boldsymbol{\omega}(t) = \boldsymbol{\omega}_g(t) + \boldsymbol{b}(t) + \boldsymbol{\eta}_{\mathrm{ARW}}(t)$, where $\mathrm{d}\boldsymbol{b}(t)/\mathrm{d}t = \boldsymbol{\eta}_{\mathrm{RRW}}(t)$. The angular rate estimate is $\hat{\boldsymbol{\omega}}(t_k) = \boldsymbol{\omega}_g(t_k) + \hat{\boldsymbol{b}}(t_k)$, and the propagation rotation vector is $\boldsymbol{a}_p = \Delta t\hat{\boldsymbol{\omega}}(t_k)$, where the time interval $\Delta t \equiv t_{k+1} - t_k$ is short enough that $\hat{\omega}$ is approximately constant. Attitude propagation when the assumption of approximately constant $\hat{\omega}$ is not valid is discussed in [24]. The propagated attitude estimate and state are $q_{\mathrm{ref}}(t_{k+1}) = q(\boldsymbol{a}_p) \otimes q_{\mathrm{ref}}(t_k)$ and $\hat{\boldsymbol{x}}_{k+1} = \hat{\boldsymbol{x}}_k$.

The discrete-time state transition matrix is given by

$$\Phi_k(t) = \begin{bmatrix} R(a_p) & S(a_p) & & & & \\ \mathbf{0}_{3\times3} & I_{3\times3} & & & & \\ & & I_{3\times3} & & & \\ & & & I_{3\times3} & & \\ & & & & I_{3\times3} & \end{bmatrix} \tag{14}$$

$$R(a) = (\cos a)I - \left(\frac{\sin a}{a}\right)[a\times] + \left(\frac{1-\cos a}{a^2}\right)aa^T \tag{15}$$

$$S(a) = \Delta t\left[\left(\frac{\sin a}{a}\right)I - \left(\frac{1-\cos a}{a^2}\right)[a\times] + \left(\frac{a-\sin a}{a^3}\right)aa^T\right] \tag{16}$$

and the propagated covariance is $P_{k+1} = \Phi_k P_k \Phi_k^T + Q_k$. The cross-product matrix $[a\times]$ is defined by $[a\times]b = a \times b$.

C. Measurement Update

The input to a measurement update phase consists of one or more observed star unit vectors $\boldsymbol{u}$ in an i, j, k sensor coordinate frame with the k axis along the line of sight and the i, j axes in the focal plane. The corresponding reference unit vectors in the celestial frame $\boldsymbol{u}'$ are computed from a star catalog. The measurement model is given by

$$y = h(\boldsymbol{u}) + \eta_y = \begin{bmatrix} h \\ v \end{bmatrix} + \eta_y = \begin{bmatrix} u_1/u_3 \\ u_2/u_3 \end{bmatrix} + \eta_y \tag{17}$$

where the measurement covariance $R = E\{\eta_y \quad \eta_y^T\} = \sigma_y^2 I$. The jth sensor attitude is $A_i^j(t) = A(a_j(t))A_b^j A_i^b(t)$, and the measurement residuals are $\Delta y \equiv h(u) - h(A(a_j(t))A_b^j A_i^b(t)u')$.

The measurement sensitivity matrix representing the relationship of the observations to the filter states is

$$H = \frac{\partial y}{\partial x} = \frac{\partial h}{\partial u}\frac{\partial \boldsymbol{u}}{\partial \boldsymbol{x}} = \frac{\partial h}{\partial u}\begin{bmatrix} \dfrac{\partial \boldsymbol{u}}{\partial \boldsymbol{a}} & \mathbf{0} & \dfrac{\partial \boldsymbol{u}}{\partial \boldsymbol{a}_{\mathrm{LRS}}} & \dfrac{\partial \boldsymbol{u}}{\partial \boldsymbol{a}_{\mathrm{IST}}} & \dfrac{\partial \boldsymbol{u}}{\partial \boldsymbol{a}_{\mathrm{BST2}}} \end{bmatrix} \tag{18}$$

where, from Eq. (17),

$$\frac{\partial h}{\partial u} = \begin{bmatrix} 1/u_3 & 0 & -u_1/u_3^2 \\ 0 & 1/u_3 & -u_2/u_3^2 \end{bmatrix} \tag{19}$$

The factors $\partial\boldsymbol{u}/\partial\boldsymbol{a}$ and $\partial\boldsymbol{u}/\partial\boldsymbol{a}_j$ represent the sensitivity of star unit vectors to body frame attitude and jth sensor alignment variations. Their derivation here follows [9,17].

For $\partial\boldsymbol{u}/\partial\boldsymbol{a}$, the jth alignment is held constant and absorbed in A_b^j. For a reference attitude $A_i^r(t)$ arbitrarily close to $A_i^b(t)$ and a small attitude error rotation vector $\boldsymbol{a}$ with the first-order approximation $A(a) \approx (I - [a\times])$, the attitude is modeled as $A_i^b(t) = (I - [a\times])A_i^r(t)$. Observed and reference unit vectors are related by $\boldsymbol{u} = A_b^j A_i^b(t)\boldsymbol{u}'$, and substitution gives

$$\boldsymbol{u} = A_b^j A_i^r(t)\boldsymbol{u}' - A_b^j[a\times]A_i^r(t)\boldsymbol{u}' \tag{20}$$

$$\boldsymbol{u} = A_b^j A_i^r(t)\boldsymbol{u}' + A_b^j[A_i^r(t)\boldsymbol{u}'\times]a \tag{21}$$

$$\partial\boldsymbol{u}/\partial\boldsymbol{a} = A_b^j[A_i^b(t)\boldsymbol{u}'\times] \tag{22}$$

for $a_i^r \to a_i^b$ as $a \to \mathbf{0}$.

For $\partial\boldsymbol{u}/\partial\boldsymbol{a}_j$ with a reference alignment A_b^r arbitrarily close to A_b^j and the approximation $A(a_j) \approx (I - [a_j\times])$, the jth sensor alignment is modeled as $A(a_j)A_b^r = (I - [a_j\times])A_b^r$. Observed and reference unit vectors are related by $\boldsymbol{u} = A(\boldsymbol{a}_j)A_b^r A_i^b(t)\boldsymbol{u}'$, and substitution gives

$$\boldsymbol{u} = A_b^r A_i^b(t)\boldsymbol{u}' - [a_j\times]A_b^r A_i^b(t)\boldsymbol{u}' \tag{23}$$

$$\boldsymbol{u} = A_b^r A_i^b(t)\boldsymbol{u}' + [A_b^r A_i^b(t)\boldsymbol{u}'\times]a_j \tag{24}$$

$$\partial \boldsymbol{u}/\partial \boldsymbol{a}_j = [A_b^j A_i^b(t)\boldsymbol{u}'\times] \tag{25}$$

for $a_b^r \to a_b^j$ as $a_j \to \mathbf{0}$.

After the propagation of the state and covariance from t_k to t_{k+1}, the measurement update at t_{k+1} is performed using the Kalman gain $K = PH^T(HPH^T + R)^{-1}$ and estimated state correction

$$\Delta\hat{\boldsymbol{x}} = [\,\Delta\hat{\boldsymbol{a}}^T \quad \Delta\hat{\boldsymbol{b}}^T \quad \Delta\hat{\boldsymbol{a}}_{\text{LRS}}^T \quad \Delta\hat{\boldsymbol{a}}_{\text{IST}}^T \quad \Delta\hat{\boldsymbol{a}}_{\text{BST2}}^T\,]^T = K\Delta y \tag{26}$$

with covariance update $P_+ = (I - KH)P_-$. The rate bias estimate is updated by $\hat{b}_+ = \hat{b}_- + \Delta\hat{b}$, and the attitude error estimate is moved into the reference attitude $q_{\text{ref}+} = q(\Delta\hat{a}) \otimes q_{\text{ref}-}$. The sensor alignments are updated by $\hat{\boldsymbol{a}}_{\text{LRS}+} = \hat{\boldsymbol{a}}_{\text{LRS}-} + \Delta\hat{\boldsymbol{a}}_{\text{LRS}}$, $\hat{\boldsymbol{a}}_{\text{IST}+} = \hat{\boldsymbol{a}}_{\text{IST}-} + \Delta\hat{\boldsymbol{a}}_{\text{IST}}$, and $\hat{\boldsymbol{a}}_{\text{BST2}+} = \hat{\boldsymbol{a}}_{\text{BST2}-} + \Delta\hat{\boldsymbol{a}}_{\text{BST2}}$.

D. Alignment Process Noise

MMAE is used to estimate alignment process noise values σ_{LRS}, σ_{IST}, and σ_{BST2} by testing a set of candidates. Each candidate is implemented in its own filter H_i and the set of candidates form a filter bank H_i; $i = 1, \ldots, n$. Simulated measurements are input to the filter bank, and the results are compared with simulation truth to select the best candidate. The description here follows [25].

The simulation represents a sensor frame as a rotation $A_i^{\text{TRK}}(t) = A(\boldsymbol{a}_{\text{TRK}}(t))A_i^r(t)$, where $A_i^r(t)$ is a reference attitude and $A(\boldsymbol{a}_{\text{TRK}}(t))$ is a rotation matrix equivalent to a small alignment rotation vector $\boldsymbol{a}_{\text{TRK}}(t)$. $A_i^r(t)$ includes the orbital rate of 223 arcseconds/s for motion of the stars through the sensor field of view. The simulation state $\boldsymbol{x}(t)$ is the sensor alignment $\boldsymbol{a}_{\text{TRK}}(t)$ and includes a sinusoidal orbital variation

$$\boldsymbol{x}(t) \equiv \boldsymbol{a}_{\text{TRK}}(t) = [\,a\ \sin(2\pi t/t_p + \theta_0) \quad 0 \quad 0\,]^T \tag{27}$$

with amplitude a, period t_p equal to the orbital period ($t_p = 5790$ s), and a random initial phase θ_0. The sensor alignment is driven by zero-mean Gaussian noise $E\{\,\eta_{\text{TRK}} \quad \eta_{\text{TRK}}^T\,\} = \sigma_{\text{TRK}}^2 I$, and the continuous-time state equation equivalent of Eq. (12) is $\delta\dot{x} = \eta_{\text{TRK}}$. The state is constant during propagation $\hat{x}_{k+1} = \hat{x}_k$ and is modeled as driven by noise alone with $Q_k = \Delta t\sigma_{\text{TRK}}^2 I$ and $P_{k+1} = P_k + Q_k$ for $\Delta t \equiv t_{k+1} - t_k$. Measurement updates are performed as in Sec. III.C except for the sensitivity matrix, which reduces to

$$H = \frac{\partial y}{\partial x} = \frac{\partial h}{\partial u}\frac{\partial u}{\partial x} = \frac{\partial h}{\partial u}\frac{\partial u}{\partial a_{\text{TRK}}} \tag{28}$$

After the propagation of the state and covariance from t_k to t_{k+1}, the measurement update at t_{k+1} is performed using the Kalman gain $K = PH^T(HPH^T + R)^{-1}$, estimated state correction $\Delta\hat{x} = \Delta\hat{\boldsymbol{a}}_{\text{TRK}} = K\Delta y$, and covariance update $P_+ = (I - KH)P_-$.

The measurement probability for a candidate and filter bank member H_i is given by

$$P(y_k|H_i) = (2\pi)^{-m/2}|S_k|^{-1/2}\exp(-\Delta y_k^T S_k^{-1}\Delta y_k/2) \tag{29}$$

where $S_k = H_k P_k H_k^T + R_k$ and m is the number of filter states. At the beginning of a simulation, each of the H_i are assigned the same probability $P_0(H_i) = n^{-1}$ of being the best. The probabilities are updated at each filter measurement update by

$$P_k(H_i) = \frac{P(y_k|H_i)P_{k-1}(H_i)}{\sum_{j=1}^n P(y_k|H_j)P_{k-1}(H_j)} \tag{30}$$

If a $P_k(H_i)$ approaches 1 as t_k increases, it is evidence that the associated filter H_i and candidate are the most correct.

Two cases are considered here with simulated alignment variation amplitudes $a_1 = 2$ and $a_2 = 10$ arcseconds. In both cases, seven candidates and filter bank members H_i; $i = 1, \ldots, 7$ are tested. The candidate values associated with the H_i are shown in the columns 2 and 4 of Table 1.

Table 1 MMAE results for alignment process noise

	$a_1 = 2$, arcseconds		$a_2 = 10$, arcseconds	
	σ_{TRK}, arcseconds/s$^{1/2}$	$P(H_i)$	σ_{TRK}, arcseconds/s$^{1/2}$	$P(H_i)$
H_1	0.002	0	0.015	0
H_2	0.005	0	0.02	0
H_3	0.007	0	0.025	0.001
H_4	0.01	1	0.03	0.985
H_5	0.015	0	0.035	0.014
H_6	0.02	0	0.04	0
H_7	0.025	0	0.045	0

Table 2 Flight data sample.

Campaign	Year	Beta angle, deg	Days	Orbits	LRS star orbits
L1A	2003S	−38.5	36.8	550	211
L2A	2003F	60	54.4	811	811
L2B	2004S	47	33.2	495	494
L3A	2004F	−53	35.8	535	535
L3B	2005S	−55.5	35.2	525	525
L3D	2005F	57	33.3	497	497
L3E	2006S	55	33.3	497	497
L3G	2006F	−49	33.3	497	497
L3H	2007S	−53.5	33.7	503	503
L3I	2007F	39	33.4	499	499
L3J	2008S	68	33.3	497	66
L2D	2008F	−49	22.2	331	331
L2E	2009S	−65	33.0	493	493

The final hypothesis probabilities $P(H_i)$ are used to select the best candidates: $\sigma_{\text{TRK}} = 0.01$ and $\sigma_{\text{TRK}} = 0.03$ arcseconds/s$^{1/2}$. The amplitudes of the line-of-sight orbital variations are on the order of 1 to 2 arcseconds for the BSTs and 10 arcseconds for the IST [8,26]. Based on alignment filter results during the portions of each orbit with LRS star observations, the LRS line-of-sight orbital variations are believed to be similar to the IST.

IV. Flight Data Sample and Data Reduction

The data sample is limited to periods when the altimetry laser system is active, referred to as laser campaigns and identified by an integer from 1 to 3 indicating the operational laser and a letter indicating the position in the sequence of campaigns for the laser. For example, laser 3B (L3B) is the second campaign to use laser 3. Laser campaigns typically cover 33 days. The flight data included in the sample consists of the 13 spring and fall laser campaigns, as shown in Table 2. The year values indicate spring or fall (S or F). The beta angle is the mean angle from the orbital plane to the sun for a campaign. The orbit is approximately circular with a 94 deg inclination, and the rate of change of the ascending node and beta angle is approximately 0.5 deg/day. The last column gives the number of orbits during

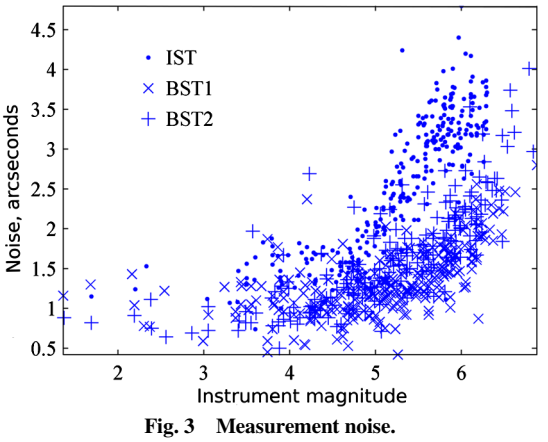

Fig. 3 Measurement noise.

which the LRS was observing stars. LRS star tracking was deactivated during L1A and L3J due to operational issues.

The data sample is publicly available from the National Snow and Ice Data Center (NSIDC) [27]. We believe that publicly available star tracker and gyro data of this nature are an important resource for the community. The ICESat star tracker and gyro data are organized in sets of files referred to as granules that cover two orbital revolutions and are identified by the prefix GLA04. The GLA04 files can be directly downloaded from the NSIDC [http://nsidc.org/data/icesat].

A. Measurement Errors

Star measurements are represented by three-dimensional unit vectors $\boldsymbol{u}$ expressed as h, v coordinates in an i, j, k sensor coordinate frame as discussed in Sec. III.C. Measurement errors include both stochastic errors (nondeterministic measurement noise) and deterministic errors (distortion or low spatial frequency error here) [28–30].

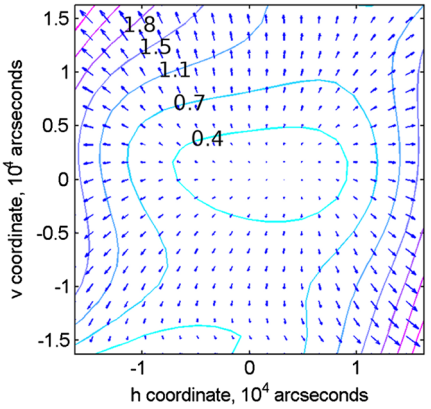

Fig. 4 Distortion corrections for the IST.

Measurement noise σ_y is estimated empirically for use in the measurement covariance $R = E\{\eta_y \quad \eta_y^T\} = \sigma_y^2 I$. The estimate is based on variations of the angular separations between pairs of stars [31]. The variance of the separations between stars a and b is equal to the sum of their individual noise variances $\sigma_{ab}^2 = \sigma_a^2 + \sigma_b^2$, where σ_{ab}^2 is calculated directly from a set of simultaneous measurements of stars a and b. For a set of simultaneous measurements of three stars a, b, and c, the variances of the separations form three equations $\sigma_{ab}^2 = \sigma_a^2 + \sigma_b^2$, $\sigma_{ac}^2 = \sigma_a^2 + \sigma_c^2$, and $\sigma_{bc}^2 = \sigma_b^2 + \sigma_c^2$ with three unknowns σ_a^2, σ_b^2, and σ_c^2. When the number of measured stars n is greater than 3 for a given time period, there is a variable number of measured angular separations m. If $m > n$, the resulting system of equations is solved using least-squares methods. The estimated noise as a function of star brightness is shown in Fig. 3.

Distortion is estimated based on measurements $y \equiv [\boldsymbol{h} \quad \boldsymbol{v}]^T$ and measurement residuals $\Delta y \equiv [\Delta \boldsymbol{h} \quad \Delta \boldsymbol{v}]^T$, which are computed as discussed in Sec. III.C. The distortion model is given by $\Delta h = h_h x + \eta_h$ and $\Delta v = h_v x + \eta_v$, where

$$h_h = [1 \quad h \quad v \quad h^2 \quad hv \quad v^2 \quad h^3 \quad h^2 v \quad hv^2 \quad v^3 \quad \mathbf{0}_{1\times 10}] \tag{31}$$

$$h_v = [\mathbf{0}_{1\times 10} \quad 1 \quad h \quad v \quad h^2 \quad hv \quad v^2 \quad h^3 \quad h^2 v \quad hv^2 \quad v^3] \tag{32}$$

For a sample of measurements and residuals, the observation vector $H^T \Delta y$ and information matrix $H^T H$ are accumulated by $(H^T \Delta y)_i =$

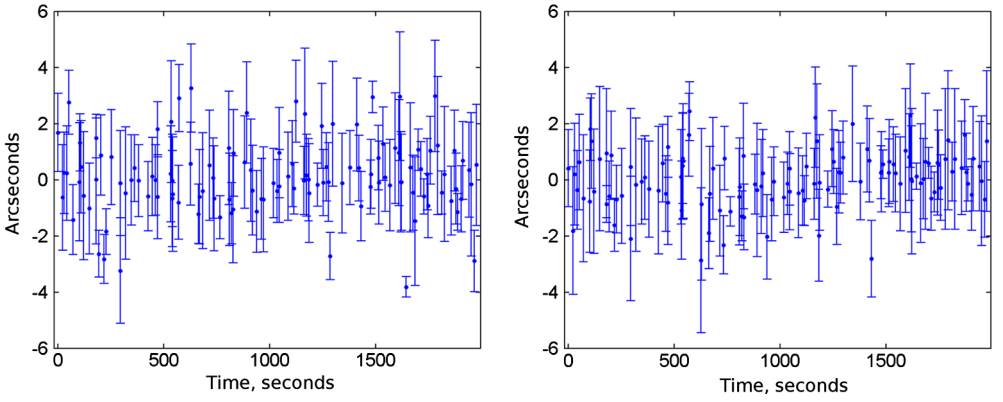

a) b)

Fig. 5 BST1 pass residuals a) $\overline{\Delta h} \pm \sigma_{\Delta h}$ and b) $\overline{\Delta v} \pm \sigma_{\Delta v}$ during a 2000 s interval from campaign L1A.

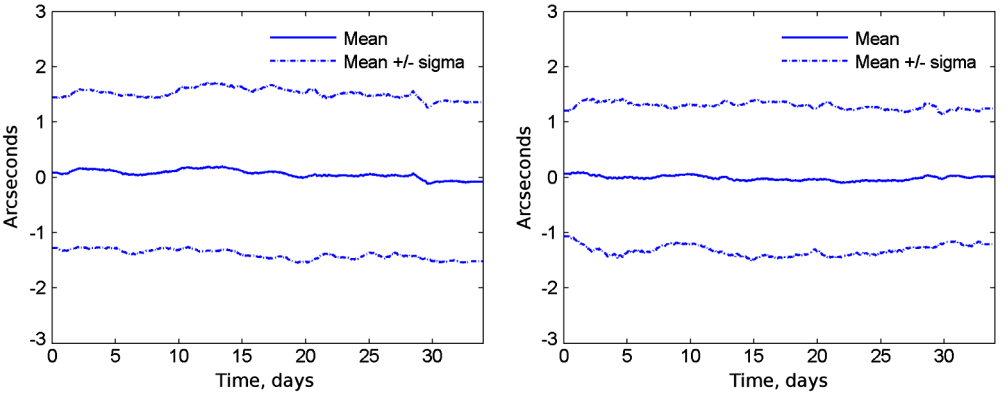

a) b)

Fig. 6 BST1 pass residuals a) $\overline{\Delta h}_k \pm \sigma_{hk}$ and b) $\overline{\Delta v}_k \pm \sigma_{vk}$ over the 36.8 days of campaign L1A.

Table 3 Pass statistics for the flight data sample

Tracker	Star passes per revolution	Observations per pass	Pass length, s	Time between pass starts, s
LRS	23 ± 5	45 ± 5	5 ± 1	88 ± 10
IST	361 ± 16	896 ± 25	94 ± 2	12 ± 1
BST1	383 ± 14	676 ± 27	69 ± 3	12 ± 1
BST2	416 ± 9	583 ± 28	62 ± 2	11 ± 1

$(H^T\Delta y)_{i-1} + h_h^T\Delta h + h_v^T\Delta v$ and $(H^TH)_i = (H^TH)_{i-1} + h_h^Th_h + h_v^Th_v$, beginning with $(H^T\Delta y)_0 = \mathbf{0}_{20\times1}$ and $(H^TH)_0 = \mathbf{0}_{20\times20}$. The least-squares estimate of the distortion parameters x is given by $\hat{\boldsymbol{x}} = (H^TH)^{-1}H^T\Delta y$.

Distortion corrections are applied to the measured star unit vectors before use in the alignment filter. The IST distortion correction map is shown in Fig. 4 as an example. The largest corrections in the corners of the field of view are approximately 2.5 arcseconds. The flight data used to estimate the corrections consists of six campaigns covering 228 days from 2003 to 2007 [30].

B. Pass Residuals and Line-of-Sight Variations

Pass residuals are used to characterize the measurements and predictions. A pass is the set of measurements of a star as it passes through a tracker field of view from acquisition to exit. Each pass is reduced from hundreds of measurements and residuals to a single record. For example, during the 37-day-long L1A laser campaign, BST1 output 116 million measurements of 151,094 passes and 1,724 unique stars. The BSTs and IST typically observe five or six passes simultaneously. The LRS observes at most one pass with significant time gaps from one pass to the next.

Pass residuals are expressed using local tangent plane coordinates, Eqs. (1–5), with the predicted unit vectors acting as the references $\boldsymbol{u}_{\text{ref}}$. The observed unit vectors are near the $\boldsymbol{u}_{\text{ref}}$, and their local tangent plane coordinates represent the measurement residuals and are approximately equivalent to angles ($h \cong \theta_h$ and $v \cong \theta_v$). For a pass with measurement residuals $\Delta y_i; i = 1, \ldots, n$, the pass residual mean and covariance are given by

$$\overline{\Delta y} \equiv [\,\overline{\Delta h} \quad \overline{\Delta v}\,]^T = \sum_{i=1}^{n} \Delta y_i/n \tag{33}$$

$$\text{cov}(\Delta y) = \sum_{j=1}^{n}((\Delta y_j - \overline{\Delta y})(\Delta y_j - \overline{\Delta y})^T)/n = \begin{bmatrix} \sigma^2_{\Delta h} & \sigma^2_{\Delta h\Delta v} \\ \sigma^2_{\Delta h\Delta v} & \sigma^2_{\Delta v} \end{bmatrix} \tag{34}$$

and are time stamped with the mean measurement time. Figure 5 shows $\overline{\Delta h} \pm \sigma_{\Delta h}$ and $\overline{\Delta v} \pm \sigma_{\Delta v}$ for 122 BST1 passes during a 2000 s interval from campaign L1A. The 122 pass means and variances are computed from 94,024 individual residuals.

Over time scales greater than hundreds of seconds, time series of $\overline{\Delta h}(t_j)$ and $\overline{\Delta v}(t_j)$ are characterized using moving averages $ma(\overline{\Delta h}(t_j))$ and $ma(\overline{\Delta v}(t_j))$. The variations in $\overline{\Delta h}(t_j)$ and $\overline{\Delta v}(t_j)$ are characterized by $\sigma_h(t_j)^2 \equiv ma([\overline{\Delta h}(t_j) - ma(\overline{\Delta h}(t_j))]^2)$ and $\sigma_v(t_j)^2 \equiv ma([\overline{\Delta v}(t_j) - ma(\overline{\Delta v}(t_j))]^2)$. The moving averages are interpolated to time series $\overline{\Delta h}_k$, $\overline{\Delta v}_k$, σ_{hk}, and σ_{vk} with constant time intervals $\Delta t = t_{k+1} - t_k$. Figure 6 shows $\overline{\Delta h}_k \pm \sigma_{hk}$ and $\overline{\Delta v}_k \pm \sigma_{vk}$ for BST1 over the 37 days of campaign L1A.

The time series $\overline{\Delta h}_k$ and $\overline{\Delta v}_k$ are further reduced to parameters $\text{mean}(|\overline{\Delta h}_k|) \pm \text{std}(\overline{\Delta h}_k)$ and $\text{mean}(|\overline{\Delta v}_k|) \pm \text{std}(\overline{\Delta v}_k)$ to

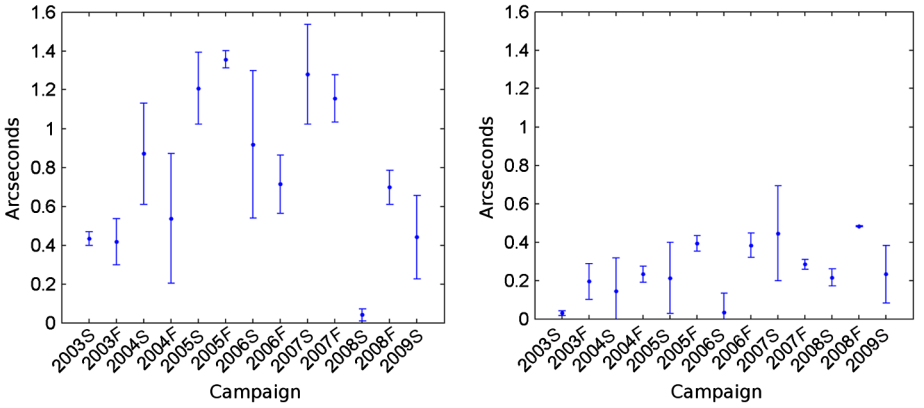

Fig. 7 LRS pass residuals a) $\text{mean}(|\overline{\Delta h}_k|) \pm \text{std}(\overline{\Delta h}_k)$ and b) $\text{mean}(|\overline{\Delta v}_k|) \pm \text{std}(\overline{\Delta v}_k)$.

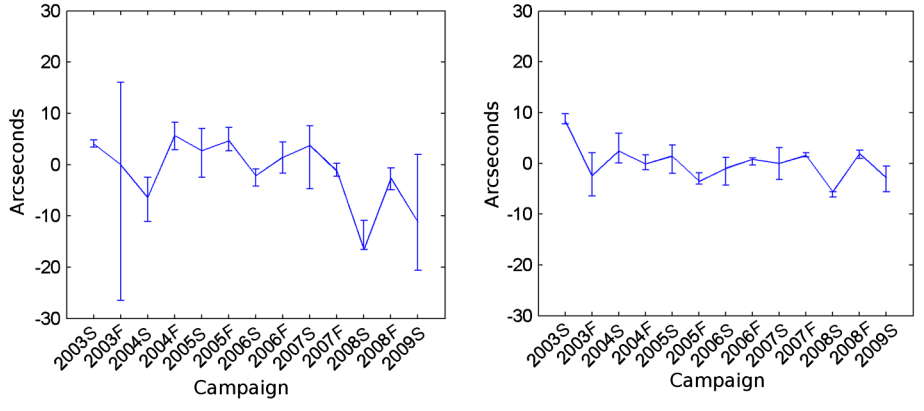

Fig. 8 LRS line-of-sight variations a) $\bar{h} \pm \Delta h$ and b) $\bar{v} \pm \Delta v$.

characterize the pass residuals over a time interval. Results for mean($|\overline{\Delta h_k}|$) and mean($|\overline{\Delta v_k}|$) that are significantly greater than zero are evidence of biases in the pass residuals. If there are biases in the pass residuals from one sensor alone, then they represent errors in the estimated alignment and line of sight in the body frame for that sensor.

Variations of a tracker line of sight are expressed using local tangent plane coordinates (Sec. II). The tracker reference alignment A_b^{TRK} defines a line of sight in the body frame that is used as the reference $\boldsymbol{u}_{\mathrm{ref}}$ for the local tangent plane coordinate frame. All of the estimated line-of-sight unit vectors are near the k axis, and the local tangent plane coordinates are approximately equivalent to angles ($h \cong \theta_h$ and $v \cong \theta_v$). The line-of-sight time series $h(t_i)$ and $v(t_i)$ are interpolated to h_k and v_k at the same times t_k and constant time intervals $\Delta t = t_{k+1} - t_k$ used for pass residuals. In the results section, variations in the h_k and v_k coordinates of a line of sight over a time interval are characterized by the medians $\bar{h} \equiv \mathrm{median}(h_k)$, $\bar{v} \equiv \mathrm{median}(v_k)$, and amplitudes $\Delta h \equiv \max(h_k) - \min(h_k)$, $\Delta v \equiv \max(v_k) - \min(v_k)$.

V. Results

The relative sparsity of LRS star observations is summarized by Table 3. There are approximately 23 LRS star passes per orbit vs hundreds for the other three trackers. The gaps between LRS passes are approximately 88 s long, not including periods in sunlight during which LRS star measurements are disabled. A typical LRS pass is approximately 5 s long and contains 45 observations.

LRS pass residuals are summarized by campaign in Fig. 7. The parameters mean($|\overline{\Delta h_k}|$) ± std($\overline{\Delta h_k}$) and mean($|\overline{\Delta v_k}|$) ± std($\overline{\Delta v_k}$) are used to characterize the differences between the LRS star measurements and the alignment filter predictions over each campaign. The mean($|\overline{\Delta h_k}|$) value for 2008S is an outlier caused by the loss of LRS star tracking after 66 orbits during the L3J campaign (Table 2).

Table 4 Pass residuals $h \equiv \mathrm{mean}(|\overline{\Delta h_k}|)$ and $v \equiv \mathrm{mean}(|\overline{\Delta v_k}|)$ in arcseconds.

	LRS		IST		BST1		BST2	
	h	v	h	v	h	v	h	v
2003S	0.4	0.0	0.0	0.2	0.1	0.0	0.1	0.0
2003F	0.4	0.2	0.2	0.0	0.1	0.0	0.0	0.1
2004S	0.9	0.1	0.1	0.1	0.1	0.0	0.0	0.0
2004F	0.5	0.2	0.1	0.1	0.0	0.1	0.1	0.2
2005S	1.2	0.2	0.0	0.2	0.1	0.0	0.1	0.0
2005F	1.4	0.4	0.1	0.0	0.1	0.0	0.0	0.0
2006S	0.9	0.0	0.0	0.1	0.1	0.1	0.0	0.0
2006F	0.7	0.4	0.1	0.2	0.0	0.2	0.1	0.2
2007S	1.3	0.4	0.1	0.1	0.1	0.0	0.1	0.0
2007F	1.2	0.3	0.3	0.0	0.1	0.0	0.0	0.0
2008S	0.0	0.2	0.1	0.1	0.0	0.0	0.0	0.0
2008F	0.7	0.5	0.0	0.2	0.0	0.2	0.0	0.2
2009S	0.4	0.2	0.0	0.2	0.0	0.1	0.0	0.1

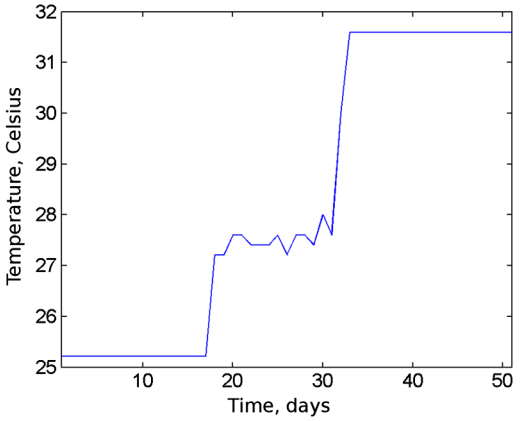

Fig. 9 Temperature variations during L2A from a thermistor associated with the LRS.

The $\overline{\Delta h_k}$ residuals are greater than the $\overline{\Delta v_k}$ residuals and are evidence of a greater LRS line-of-sight variation in the h direction. There are two other possible contributors to this difference. Because the pitch axis is aligned with the body frame x axis, the gyro rate $\boldsymbol{\omega}_g(t_k)$ about the x axis is 223 arcseconds/s, and the rate about the y axis is approximately zero. The v coordinates of star measurements change at a rate of 223 arcseconds/s, and the h coordinates are approximately constant. The possible effects of these geometric asymmetries on attitude estimation uncertainties are also noted in [8].

LRS line-of-sight variations are shown by campaign in Fig. 8. The parameters $\bar{h}$, Δh, $\bar{v}$, and Δv are shown as $\bar{h} \pm \Delta h$ and $\bar{v} \pm \Delta v$ to characterize the line-of-sight variations during and between each campaign. A constant bias equal to the median value has been removed from the $\bar{h}$ and $\bar{v}$ time series. The variations in the h direction are larger than those in the v direction. The h variations during the 2003F and 2009S (L2A and L2E) campaigns have particularly large amplitudes, and these two campaigns are discussed in more detail in the following text.

Pass residuals are summarized by tracker and campaign in Table 4. Column headings h and v are used for the parameters mean($|\overline{\Delta h_k}|$) and mean($|\overline{\Delta v_k}|$). The IST, BST1, and BST2 pass residuals are on the order of 0.0 to 0.2 arcseconds, and the LRS residuals are significantly larger. The parameters mean($|\overline{\Delta h_k}|$) ± std($\overline{\Delta h_k}$) and mean($|\overline{\Delta v_k}|$) ± std($\overline{\Delta v_k}$) could be given in Table 4, but the values of std($\overline{\Delta h_k}$) and std($\overline{\Delta v_k}$) are relatively small (0.0 or 0.1 in all cases) except for the LRS. The LRS std($\overline{\Delta h_k}$) and std($\overline{\Delta v_k}$) values are shown in Fig. 7.

Line-of-sight variations are summarized by tracker and campaign in Table 5. The parameters $\bar{h}$, Δh, $\bar{v}$, and Δv are used to characterize the line-of-sight variations during and between each campaign. A constant bias equal to the median value has been removed from each $\bar{h}$ and $\bar{v}$ time series. The variation amplitudes Δh for both the LRS and

Table 5 Line-of-sight variations $\bar{h} \pm \Delta h$ and $\bar{v} \pm \Delta v$ in arcseconds.

	LRS				IST				BST2			
	$\bar{h}$	Δh	$\bar{v}$	Δv	$\bar{h}$	Δh	$\bar{v}$	Δv	$\bar{h}$	Δh	$\bar{v}$	Δv
2003S	4	1.4	8.4	2	12.2	2.5	−10.2	1.2	0	2.4	2.9	0.1
2003F	0	42.5	−2.4	8.6	−2.4	24.5	2.2	27.7	−1.6	4.5	0.5	1.8
2004S	−6.4	8.5	2.4	5.8	8.3	5.8	−10.9	3.7	−0.7	2.9	0.7	0.3
2004F	5.6	5.3	−0.1	3	0	6.1	−0.5	1.6	−1.8	4.6	0.6	0.3
2005S	2.7	9.6	1.4	5.5	3	5.8	0.3	3	−1.5	0.9	0.7	0.4
2005F	4.7	4.6	−3.5	2.2	−2.3	7.4	2.2	4.6	0.8	2.6	−0.5	0.7
2006S	−2.2	3.3	−1	5.5	2.2	10.4	−4.7	4	0.6	2	0	0.6
2006F	1.4	6.1	0.8	1.4	−2.7	6.2	4.3	0.9	−0.8	2.6	0	0.6
2007S	3.7	12.3	0	6.3	0.4	3.4	0	3.3	−0.6	2.7	0.4	0.4
2007F	−1.3	2.5	1.5	0.8	3.7	5.3	0.5	2.1	1.9	2.7	−0.3	0.3
2008S	−16.5	5.6	−5.7	1	−22.4	21.5	−8.1	1.7	2.3	1.6	−1.5	1.6
2008F	−2.7	4.2	1.9	1.6	−5.1	2	0.2	1.3	0.1	2.7	−0.5	0.2
2009S	−11.2	22.6	−2.9	5.1	−18.2	25.8	−4.8	3.6	0.4	2	−0.9	1.9

IST are relatively large during the 2003F and 2009S (L2A and L2E) campaigns, as noted for the LRS alone in Fig. 8. Because of the pattern in the $\bar{h}$ and Δh values, we believe that the 2008S (L3J) campaign is a similar case, but LRS star tracking was lost after 66 orbits during L3J, and there is effectively poor sampling of the Δh value.

Campaign L2A is unique in being relatively long (54 days) and containing two GLAS temperature events caused by configuration commands from the ground. The temperature changes effectively divide L2A into three subcampaigns. Temperature variations from a thermistor associated with the LRS are shown in Fig. 9.

Line-of-sight variations for the LRS, IST, and BST2 are shown in Fig. 10. The time series h_k and v_k for each line of sight are plotted. A constant bias equal to the median value has been removed from each time series. Pass residuals for all four star trackers (including BST1) are shown in Fig. 11. The time series $\overline{\Delta h}_k$ and $\overline{\Delta v}_k$ for each tracker are plotted. The time series $\overline{\Delta h}_k \pm \sigma_{hk}$ and $\overline{\Delta v}_k \pm \sigma_{vk}$ could be plotted here, but the σ_{hk} and σ_{vk} series are relatively constant and obscure the bias information represented by $\overline{\Delta h}_k$ and $\overline{\Delta v}_k$. There is relatively little change of the BST2 line of sight over L2A. This agrees with its overall stability for all 13 campaigns shown in Table 5. The residuals from both BST1 and BST2 are also relatively small. The line-of-sight stability and small residuals are evidence of relatively small alignment and attitude estimate uncertainties for the BSTs.

There are strong correlations between the LRS and IST line-of-sight variations and the temperature changes in Fig. 9. There are also correlations between the LRS and IST line-of-sight h_k time series. The h_k correlations are clear during L2E (Fig. 12).

The results in [8] provide evidence that the alignment between the LRS and the GLAS optical bench is relatively stable, implying that

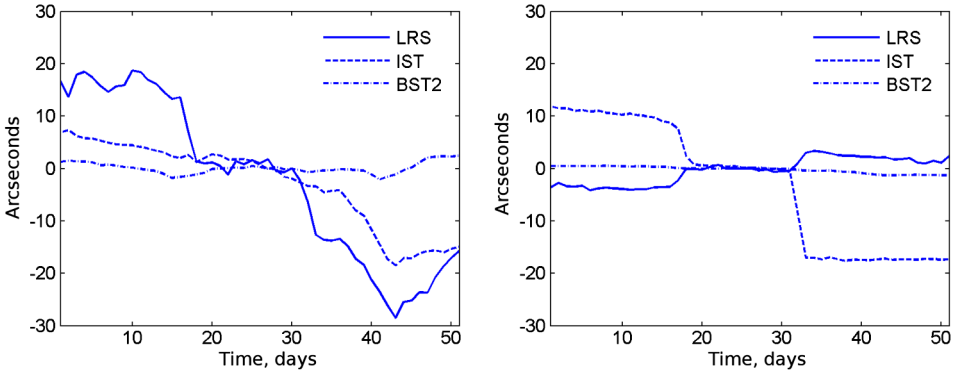

Fig. 10 Line-of-sight variations a) h_k and b) v_k during L2A.

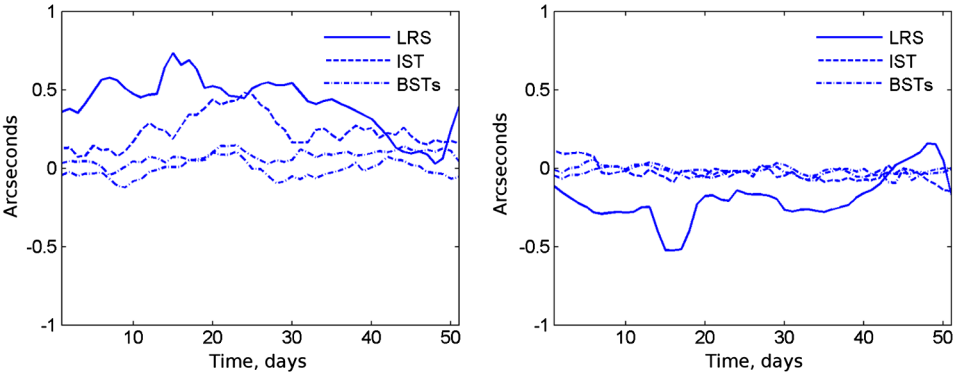

Fig. 11 Pass residuals a) $\overline{\Delta h}_k$ and b) $\overline{\Delta v}_k$ during L2A.

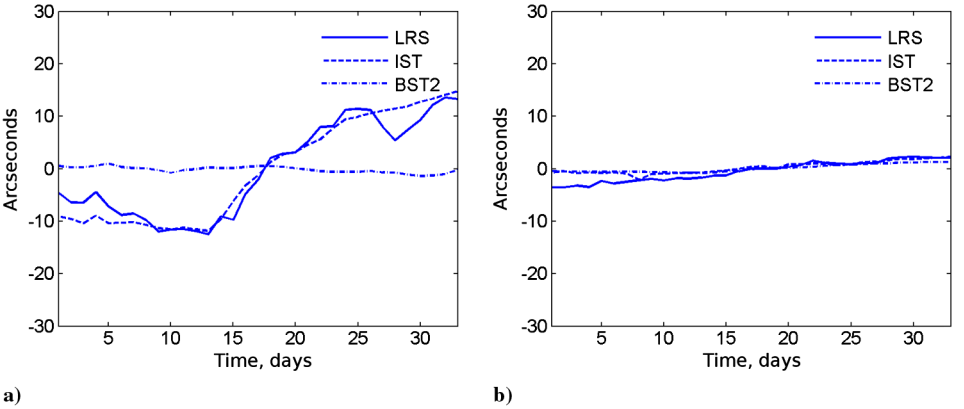

Fig. 12 Line-of-sight variations a) h_k and b) v_k during L2E.

the LRS coordinate frame is a good proxy for the GLAS coordinate frame and that the LRS line-of-sight h_k variations describe GLAS optical bench motion relative to the BSTs and spacecraft bus. The IST is correlated with the LRS by the optical bench. Also shown in [8] and [32] is that there is significant motion of the IST relative to the LRS and optical bench and that their correlation is typically partial.

VI. Conclusions

The sparse star observations from the laser reference sensor and the failure of the alignment reference signal on orbit provide strong motivation to take advantage of the information from all four star trackers when possible. The results here demonstrate that alignment filtering can provide adequate predictions of the laser reference sensor star observations for meeting the altimetry science pointing requirements. However, there are significantly higher alignment filter measurement residuals for the laser reference sensor than for the other three star trackers. Nonzero mean measurement residuals indicate that the filter alignment estimates for the laser reference sensor include biases on the order of 0.5 to 1.5 arcseconds over time scales greater than the orbital period, particularly in the direction of the body frame x axis. The biases can be reduced by increasing the alignment process noise and therefore the sensitivity of the alignment states, but the current alignment process noise parameter estimates are believed to be realistic. The biases are believed to simply reflect the limited stellar data output from the laser reference sensor. In practice, the biases are corrected in later processing phases [32].

On the other hand, the alignment filter is able to track laser reference sensor alignment variations of up to 40 arcseconds to within approximately 1 arcsecond. The filter provides laser reference sensor attitude estimates with adequate accuracy over time scales longer than the orbital period, along with tracking of large laser reference sensor and instrument star tracker alignment variations. Correlations in these variations are believed to be evidence of significant relative motion between the science instrument optical bench and the spacecraft bus. The small measurement residuals and alignment variations for the bus star trackers indicate that their alignments are stable. Together with the large and partially correlated alignment variations of the star trackers on the science instrument optical bench, they are also believed to imply that the bus star tracker coordinate frames are good proxies for both the bus frame and the alignment filter body frame.

Acknowledgment

This research was supported by NASA Grant NNX09AG20G.

References

[1] Brenner, A. C., DiMarzio, J. P., and Zwally, H. J., "Precision and Accuracy of Satellite Radar and Laser Altimeter Data Over the Continental Ice Sheets," *IEEE Transactions on Geosciences and Remote Sensing*, Vol. 45, No. 2, 2007, pp. 321–331. doi:10.1109/TGRS.2006.887172

[2] Luthcke, S. B., Rowlands, D. D., McCarthy, J. J., Pavlis, D. E., and Stoneking, E., "Spaceborne Laser-Altimeter-Pointing Bias Calibration from Range Residual Analysis," *Journal of Spacecraft and Rockets*, Vol. 37, No. 3, 2000, pp. 374–384. doi:10.2514/2.3571

[3] Luthcke, S. B., Carabajal, C. C., and Rowlands, D. D., "Enhanced Geolocation of Spaceborne Laser Altimeter Surface Returns: Parameter Calibration from the Simultaneous Reduction of Altimeter Range and Navigation Tracking Data," *Journal of Geodynamics*, Vol. 34, No. 3, 2002, pp. 447–475. doi:10.1016/S0264-3707(02)00047-9

[4] Bae, S., and Schutz, B. E., "Laser Pointing Determination Using Stellar Reference System in Geoscience Laser Altimeter System," *AAS/AIAA Space Flight Mechanics Meeting, Advances in the Astronautical Sciences*, Vol. 105, Univelt, San Diego, CA, 2000, pp. 367–382; also American Astronautical Society Paper 2000-123.

[5] Schutz, B. E., Zwally, H. J., Shuman, C. A., Hancock, D., and DiMarzio, J. P., "Overview of the ICESat Mission," *Geophysical Research Letters*, Vol. 32, No. 21, 2005, pp. 1–4. doi:10.1029/2005GL024009

[6] Bae, S., Smith, N., and Schutz, B. E., "ICESat-1 Precision Pointing Determination Algorithm Theoretical Basis Document," Center for Space Research, NASA TM-2102-208641, Austin, TX, 2012.

[7] Bae, S., Schutz, B. E., and Sirota, J. M., "ICESAT/GLAS Laser Pointing Determination," *AAS/AIAA Spaceflight Mechanics Meeting, Advances in the Astronautical Sciences*, Vol. 112, Univelt, San Diego, CA, 2002, pp. 359–370; also American Astronautical Society Paper 2002-126.

[8] Smith, N., Bae, S., Webb, C., and Schutz, B. E., "Laser Reference Sensor Alignment Estimation from Reference Signal Observations," *Journal of Spacecraft and Rockets*, Vol. 51, No. 1, 2014, pp. 48–56. doi:10.2514/1.A32546

[9] Pittelkau, M. E., "Kalman Filtering for Spacecraft System Alignment Calibration," *Journal of Guidance, Control, and Dynamics*, Vol. 24, No. 6, 2001, pp. 1187–1195. doi:10.2514/2.4834

[10] Pittelkau, M. E., "Survey of Calibration Algorithms for Spacecraft Attitude Sensors and Gyros," *AAS Astrodynamics Specialist Conference, Advances in the Astronautical Sciences*, Vol. 129, Univelt, San Diego, CA, 2007; also American Astronautical Society Paper 2007-295.

[11] Gray, C. W., Herman, L. K., Kolve, D. I., and Westerlund, G. L., "On-Orbit Attitude Reference Alignment and Calibration," *AAS Guidance and Control Conference*, Vol. 72, Univelt, San Diego, CA, 1990, pp. 275–292; also American Astronautical Society Paper 1990-042.

[12] Bayard, D. S., "An Overview of the Pointing Control System for NASA's Space Infra-Red Telescope Facility (SIRTF)," *AIAA Guidance, Navigation, and Control Conference*, AIAA Paper 2003-5832, 2003.

[13] Bayard, D. S., and Kang, B. H., "A High-Order Kalman Filter for Focal Plane Calibration of NASA's Space Infrared Telescope Facility (SIRTF)," *AIAA Guidance, Navigation, and Control Conference*, AIAA Paper 2003-5824, 2003.

[14] Li, R., Needelman, D., Fowell, R., Tsao, T.-C., and Wu, Y.-W., "Reusable Stellar Inertial Attitude Determination (SIAD) Design For Spacecraft Guidance, Navigation and Control," *AIAA Guidance, Navigation, and Control Conference*, AIAA Paper 2005-5928, 2005.

[15] Li, R., and Wu, Y.-W., "Absolute and Relative Attitude Determination for Multiple Payloads On Spacecraft," *AIAA Guidance, Navigation, and Control Conference*, AIAA Paper 2006-6048, 2006.

[16] Pittelkau, M. E., "A Kalman Filter Approach to System Alignment Calibration," *AAS/AIAA Space Flight Mechanics Meeting*, American Astronautical Society Paper 2000-127, 2000.

[17] Pittelkau, M. E., "Everything Is Relative In Spacecraft System Alignment Calibration," *Journal of Spacecraft and Rockets*, Vol. 39, No. 3, 2002, pp. 460–466. doi:10.2514/2.3830

[18] Pittelkau, M. E., and Dellinger, W. F., "Attitude Sensor Alignment And Calibration For The TIMED Spacecraft," *AAS/AIAA Space Flight Mechanics Meeting*, American Astronautical Society Paper 2003-153, 2003.

[19] O'Shaughnessy, D., and Pittelkau, M. E., "Attitude Sensor and Gyro Calibration for Messenger," NASA International Symposium on Space Flight Dynamics, NASA Conference Proceedings, NASA CP-2007-214158, 2007.

[20] Pittelkau, M. E., and O'Shaughnessy, D., "Gyro Misalignment Decomposition Applied To Messenger Calibration," *AAS Spaceflight Mechanics Meeting, Advances in the Astronautical Sciences*, Vol. 134, Univelt, San Diego, CA, 2009, pp. 1527–1539; also American Astronautical Society Paper 2009-203.

[21] Bayard, D. S., Kang, B. H., Brugarolas, P. B., and Broussalis, D., "Focal Plane Calibration of the Spitzer Space Telescope," *IEEE Control Systems*, Vol. 29, No. 6, 2009, pp. 47–70. doi:10.1109/MCS.2009.934466

[22] Markley, F. L., "Attitude Error Representation for Kalman Filtering," *Journal of Guidance, Control, and Dynamics*, Vol. 26, No. 2, 2003, pp. 311–317. doi:10.2514/2.5048

[23] Pittelkau, M. E., "Rotation Vector in Attitude Estimation," *Journal of Guidance, Control, and Dynamics*, Vol. 26, No. 6, 2003, pp. 855–860. doi:10.2514/2.6929

[24] Savage, P. G., "Strapdown Inertial Navigation Integration Algorithms Design Part 1: Attitude Algorithms," *Journal of Guidance, Control, and Dynamics*, Vol. 21, No. 1, 1998, pp. 19–28. doi:10.2514/2.4228

[25] Hanlon, P. D., and Maybeck, P. S., "Multiple-Model Adaptive Estimation Using a Residual Correlation Kalman Filter Bank," *IEEE Aerospace and Electronic Systems Magazine*, Vol. 36, No. 2, 2000, pp. 393–406. doi:10.1109/7.845216

[26] Bae, S., Webb, C., and Schutz, B. E., "Star Tracker Misalignment Calibration for the ICESat Mission," *AAS/AIAA Space Flight*

Mechanics, Advances in the Astronautical Sciences, Vol. 124, Univelt, San Diego, CA, 2006, pp. 113–124; also American Astronautical Society Paper 2006-107.

[27] Zwally, H. J., Schutz, B. E., Bentley, J., Bufton, T., Herring, J., Minster, J., Spinhirne, J., and Thomas, R., *GLAS/ICESat L1A Global Laser Pointing Data V031 [digital media]*, National Snow and Ice Data Center, Boulder, CO, 2003.

[28] Lam, Q. M., Woodruff, C., Ashton, S., and Martin, D., "Noise Estimation for Star Tracker Calibration and Enhanced Precision Attitude Determination," *IEEE Information Fusion Conference, IEEE Conference Proceedings*, Annapolis, MD, 2002, pp. 235–242.

[29] Fowell, R. A., Smith, N., Bae, S., and Schutz, B. E., "Bad Stars," *AAS Guidance and Control Conference, Advances in the Astronautical Sciences*, Vol. 133, Univelt, San Diego, CA, 2009, pp. 20–36; also American Astonautical Society Paper 2009-012.

[30] Smith, N., Bae, S., and Schutz, B. E., "Biased Star Tracker Measurements of Forty-Nine Stars from Flight Data," *Journal of Spacecraft and Rockets*, Vol. 47, No. 6, 2010, pp. 1023–1028. doi:10.2514/1.49412

[31] Lauer, M., Jauregui, L., and Kielbassa, S., "Operational Experience with Autonomous Star Trackers on ESA Interplanetary Spacecraft," Proceedings of the 20th International Symposium on Space Flight Dynamics, NASA CP-2007-214158, 2007.

[32] Luthcke, S. B., Rowlands, D. D., Williams, T. A., and Sirota, J. M., "Reduction of ICESat Systematic Geolocation Errors and the Impact on Ice Sheet Elevation Change Detection," *Geophysical Research Letters*, Vol. 32, No. 21, 2005, pp. 1–4. doi:10.1029/2005GL023689

C. Kluever
Associate Editor